LA-UR-18-25086 (Accepted Manuscript)

Radiation Belt “Dropouts” and Drift-Bounce Resonances in Broadband Electromagnetic Waves

Chaston, C.
Bonnell, J.
Wygant, J.
Reeves, Geoffrey D.
Baker, D. N.
Melrose, D.

To be published in: Geophysical Research Letters

DOI to publisher's version: 10.1002/2017GL076362

Permalink to record: http://permalink.lanl.gov/object/view?what=info:lanl-repo/lareport/LA-UR-18-25086

Radiation belt "dropouts" and drift-bounce resonances in broadband electromagnetic waves

C. C. Chaston[1], J. W. Bonnell[1], J. R. Wygant[2], G. D. Reeves[3], D. N. Baker[4] and D. B. Melrose[5].

[1] Space Sciences Laboratory, University of California, Berkeley, CA, USA

[2] Department of Physics and Astronomy, University of Minnesota, Minneapolis, MN, USA.

[3] Los Alamos National Laboratory, Los Alamos, NM, USA,

[4] Laboratory for Atmospheric and Space Physics, University of Colorado, Boulder, Co, USA

[5] School of Physics, University of Sydney, Camperdown, NSW, Australia

Corresponding author: Christopher Chaston (ccc@ssl.berkeley.edu)

Key Points:

- Kinetic eigenmodes of the geomagnetic field may deplete the outer radiation belt during the main phase of geomagnetic storms.
- Drift-bounce resonances with the wave magnetic field can drive radial diffusion on timescales less than a drift period.
- Broadband electromagnetic waves commonly observed in the inner magnetosphere during geomagnetic storms may be an important unrecognized driver of radiation belt dynamics.

This article has been accepted for publication and undergone full peer review but has not been through the copyediting, typesetting, pagination and proofreading process which may lead to differences between this version and the Version of Record. Please cite this article as doi: 10.1002/2017GL076362

Abstract

Observations during the main phase of geomagnetic storms reveal an anti-correlation between the occurrence of broadband low frequency electromagnetic waves and outer radiation belt electron flux. We show that the drift-bounce motion of electrons in the magnetic field of these waves leads to rapid electron transport. For observed spectral energy densities it is demonstrated that the wave magnetic field can drive radial diffusion via drift-bounce resonance on timescales less than a drift orbit. This process may provide outward transport sufficient to account for electron "dropouts" during storm main phase and more generally modulate the outer radiation belt during geomagnetic storms.

1 Introduction

The rapid and irreversible depletion or 'dropout' of radiation belt electron fluxes during geomagnetic storms presents a special challenge to understanding particle transport and scattering in Earth's magnetosphere [Mauk et al., 2012]. While these electrons are ultimately lost through the magnetopause [Ukhorskiy et al 2006], and to the atmosphere [Millan et al., 2010] the manner through which radiation belt electrons are transported outward to the magnetopause [Turner et al., 2012] or scattered into the atmospheric loss cone [Millan and Thorne 2007; Millan et al., 2012] remains contentious [Ukhorskiy et al., 2015].

Our interest here is the transport process. Radial transport has been explained as the consequence of outward motion of electron guiding centers due to magnetospheric compression [Shprits et al., 2006], enhanced dawn-dusk electric fields [Nishimura et al., 2007] and/or radial diffusion driven by ULF waves [Brautigam and Albert, 2000; Elkington et al., 2003; Hudson et al., 2008; Lotoaniu et al., 2010;]. For diffusive transport the rapid depletion of radiation belt phase space density characteristic of 'dropouts' requires large radial diffusion coefficients (D_{LL}). Observations indicate order of magnitude decreases in radiation belt fluxes on timescales of the order of hours [Morley et al., 2010; Turner et al, 2014; Ukhorskiy et al., 2015; Baker et al., 2016; Zhang et al., 2016; Ozeke et al., 2017]. These timescales suggest $D_{LL} > 10^{-4}$ s^{-1}. With the exception of 'shock-like' events [Li et al. 1993] these values are larger than most D_{LL} estimates from drift-resonance in MHD modes within geosynchronous orbit [Brautigam and Albert, 2000; Elkington et al., 2003; Fei et al., 2006; Huang et al., 2010; Ozeke et al., 2014, 2017; Li et al., 2016].

The nearly continuous presence of broadband low frequency electromagnetic waves in the inner magnetosphere during storm main phase [Chaston et al., 2015] suggests a possible role for these field variations in rapid radiation belt losses. Wave dispersion and propagation

analyses have shown these variations to be a broad k-spectrum of kinetic Alfvén waves with phase characteristics often indicative of standing eigenmodes or resonances. It has also been shown that the electric fields of these kinetic field-line resonances (KFLRs) can drive diffusion across L-shells [Chaston et al., 2017; from hereon, C2017]. However, for observed electric field spectral energy densities this mechanism is insufficient alone to account for main phase "dropouts" mentioned above [C2017].

To further investigate the role of broadband electromagnetic waves in main phase electron "dropouts" we now consider the action of the wave magnetic field on electron orbits. We begin by presenting a case study showing anti-correlation between broadband electromagnetic waves and radiation belt fluxes during storm main phase suggestive of the action of these waves in radiation belt depletion. We then extend the modelling of C2017 to include the contribution of the Lorentz force arising from the drift-bounce motion of electron guiding centers in the radial component of the wave magnetic field. The importance of this interaction was first suggested by Dungey [1964]. It is shown that for radiation belt electrons this force is more than an order of magnitude larger than that due to the wave electric field on which the calculations in C2017 were based. For observed spectra it is demonstrated that the wave magnetic field will drive radial transport at MeV energies on timescales of the order of minutes. Based on these estimates, and the prevalence of these modes during storm main phase, we suggest that KFLRs, or more generally broadband electromagnetic waves, may play a significant role in the rapid depletion or "dropout" of the outer radiation belt at the commencement of geomagnetic storms.

2 Observations

Figure 1 shows measurements recorded from two consecutive orbits of Van Allen Probe A: the first prior to storm commencement and the second during the main phase of the large geomagnetic storm of 27th August 2014. Apogee for these equatorial orbits occurs on the flanks

near dawn at $L \approx 6$. At this location the X and Y GSE components of the electric and magnetic field spectra shown in Figures 1b and c correspond to azimuthal (E_X) and radial (B_Y) oscillations about the Earth respectively. In Figure 1b the electric field spectra has been constructed under the assumption that $E \cdot B \approx 0$ with the blank portions in both E_X and B_Y spectra corresponding to times when the measurements are not reliable over the frequency range shown. For presenting wave spectral measurements, the $E \cdot B \approx 0$ assumption is sufficient for low frequency waves of this type. Horizontal lines in the spectrograms at constant frequency correspond to residual spacecraft spin tones.

The outstanding feature of the spectral measurements shown in Figure 1b and c is the absence of significant geophysical spectral energy densities pre-storm followed by the appearance of intense broadband field variations ($\varepsilon_B \sim 1\, nT^2/Hz$ *and* $\varepsilon_E \sim 10^3\, (\frac{mV}{m})^2/Hz$ at 0.2 Hz) ~ 8 hours later during storm main phase. From Van Allen Probe B measurements (Supplementary Figure) we know that this activity began at least 3 hours earlier with the first decrease in *Dst* at storm onset. Coincident with these field variations Figure 1e and f reveal order of magnitude increases in differential particle flux at energies up to 100 keV. These fluxes comprise the plasmas supporting the observed wave activity. On the other hand, an almost complete depletion of electron fluxes above 100 keV is apparent in Figures 1d and e – i.e. the outer radiation belt has disappeared with the appearance of the broadband wave activity. Comparison of the pitch angle plots, shown in Figures 1g-p to the wave spectra in Figures 1b and c make clear the anti-correlation in occurrence of broadband field fluctuations and relativistic electrons at all pitch angles all the way up to 4 MeV - the upper limit of the pre-storm radiation belt.

Cross spectral and dispersion analyses of broadband low frequency wave spectra of the kind shown in Figures 1a and b have revealed that the observed field variations are well described as a Doppler shifted k-spectrum of kinetic Alfvén waves often appearing as eigenmodes of the

geomagnetic field or KFLRs [Chaston et al., 2014]. The same spectral analyses have been applied to the field variations shown here and confirm the identification for this case. Because these spectral characteristics have already been detailed in statistical studies [Chaston et al., 2015] we do not represent the results here. However, with this identification in hand we now exploit the properties of KFLRs to assess the efficacy of the radial wave magnetic field in broadband electromagnetic waves for driving transport via drift-bounce resonance.

3 Drift-Bounce and the Lorentz Force

A gyrating electron moving along a geomagnetic field-line in slowly varying electromagnetic fields will drift with velocity,

$$\boldsymbol{v_d} = \frac{1}{q_e}\frac{\boldsymbol{F}\times\boldsymbol{B}}{B^2} \quad (1)$$

for $v_d \ll c$ where F is the force acting on the particle, B is the magnetic field and q_e is the electron charge. In an unperturbed dipolar magnetosphere with field strength B_o the first order drift is azimuthal. However, in the presence of an azimuthal electric field ($\boldsymbol{E_\phi}$) and/or variations in the magnetic field component normal to an L-shell ($\boldsymbol{b_\nu}$) the Lorentz force

$$\boldsymbol{F_\phi} = q_e(\boldsymbol{E_\phi} + \boldsymbol{v_\mu} \times \boldsymbol{b_\nu}) \quad (2)$$

will drive a radial drift – i.e. across L-shells. Here ν, ϕ and μ are the coordinates in L, azimuth and along B_o respectively with v_μ the electron velocity along the dipolar field-line (Cummings et al., 1969). For periodic variations in E_ϕ and b_ν secular transport across L-shells is possible for electrons satisfying,

$$\omega - m\omega_d = n\omega_b \quad (3)$$

where ω is the wave frequency, m is the azimuthal wavenumber, ω_d is azimuthal drift frequency, n is the bounce harmonic and ω_b is the bounce frequency. The transport can be

inward or outward depending on the relative phasing of the resonant electron and the wave, however in the presence of gradients of phase space density in L there will be a net diffusive flux to regions of lower phase space density [Schulz and Lanzerotti, 1974]. The operation of this transport process is especially likely between KFLRs and radiation belt electrons because the azimuthal electron drift over a bounce period is of the order of the bulk ion gyro-radius (ρ_i) outside the plasmapause – i.e. similar to the azimuthal wave scale. In fact, C2017 demonstrated that the broad spectrum of KFLRs allow satisfaction of Equation 3 over the full range of electron energies comprising the outer radiation belt.

Radial transport due to F_ϕ provides energization perpendicular to the geomagnetic field consistent with the 1st adiabatic invariant [Elkington et al., 2006] and is accompanied by acceleration along the geomagnetic field due to the parallel Lorentz force,

$$\boldsymbol{F_\mu} = q_e(\boldsymbol{E_\mu} - \boldsymbol{v_\phi} \times \boldsymbol{b_v}) \quad (4)$$

For times-scales longer than a gyro-period $\boldsymbol{v_\phi}$ can be replaced by the azimuthal drift velocity ($v_{d\phi}$) so that the total time rate of change of electron energy ($\mathcal{E}$) is,

$$\frac{d\mathcal{E}}{dt} = \boldsymbol{F} \cdot \boldsymbol{v} = q_e\,(\boldsymbol{E_\phi} + \boldsymbol{v_\mu} \times \boldsymbol{b_v}) \cdot \boldsymbol{v_{d\phi}} + q_e(\boldsymbol{E_\mu} - \boldsymbol{v_{d\phi}} \times \boldsymbol{b_v}) \cdot \boldsymbol{v_\mu} \quad (5)$$

The contributions due to $\boldsymbol{v} \times \boldsymbol{b}$ described by the 2nd and 4th terms on the right-hand side cancel to provide no energy change. However, the balance between energization across and along the geomagnetic field defined by these terms modifies the particle pitch-angle with transport across L-shells. For bouncing radiation belt electrons in KFLRs $\left|\boldsymbol{v_\mu} \times \boldsymbol{b_v}\right| \gg |\boldsymbol{E}|$ (see section 4) so that the transport and variation in pitch-angle is largely defined by action of $\boldsymbol{v} \times \boldsymbol{b}$ and given by conservation of the 1st adiabatic invariant and energy. For this case $(L + \Delta L)^3\, sin^2(\alpha_{eq} + \Delta\alpha_{eq}) \approx constant$ or,

$$\Delta\alpha_{eq} \approx tan^{-1}\left[\frac{\beta - tan\alpha_{eq}}{1+\beta tan\alpha_{eq}}\right] \text{ where } \beta = \sqrt{\frac{L^3 sin^2\alpha_{eq}}{(L+\Delta L)^3 - L^3 sin^2\alpha_{eq}}} \quad (6)$$

with $\Delta\alpha_{eq}$ the change in equatorial pitch-angle for radial transport by amount ΔL and $B_o \propto L^{-3}$ at the equator**.** Outward transport will therefore drive a shift in electron pitch angle toward the loss cone while the parallel energization due to $\boldsymbol{F_\mu}$ means that even electrons with $\alpha_{eq} \to 90^o$ (i.e. $\boldsymbol{v_\mu} \to 0$) will be subject to radial transport driven by $\boldsymbol{v_\mu} \times \boldsymbol{b_\nu}$ due to the gain in $\boldsymbol{v_\mu}$**.** These parallel dynamics may stimulate losses to the atmosphere at small α_{eq} while simultaneously increasing outward radial transport at large α_{eq} to help facilitate the all pitch-angle depletion shown in Figure 1.

4 Radial Diffusion Coefficients

The efficacy of the transport process due to $\boldsymbol{E_\phi}$ in Equation 2 was quantified in C2017 via the evaluation of radial diffusion coefficients (D_{LL}). The corresponding contribution from $\boldsymbol{v_\mu} \times \boldsymbol{b_\nu}$ can be estimated from the result for $\boldsymbol{E_\phi}$ by noting in the local case for kinetic Alfvén waves that $E_\phi/b_\nu \approx V_A\sqrt{1 + k_\phi^2\rho_i^2}$. Here V_A is the Alfvén speed, $k_\phi \approx m/rsin\theta$ where r is radial distance and θ co-latitude. This expression has been shown to provide a good statistical model for the observed relationship between electric and magnetic fields in these waves near the equator from the Van Allen Probes [Chaston et al., 2014; 2015]. Consequently at $k_\phi\rho_i = 1$ we can write,

$$\left|\frac{v_\mu \times b_\nu}{E_\phi}\right| \approx \frac{v_\mu}{\sqrt{2}V_A} \quad (7)$$

Figure 2a shows this ratio as a function of pitch angle (α) and energy at $L \approx 6$ and close to the equator where $V_A \approx 4 \times 10^6$ m/s. Here it should be noted that E_ϕ/b_ν corresponds to the Fourier amplitude and so is independent of the mode structure along B_0. For electrons with $\alpha < 90^o$

and energies above a few hundred eV, $\boldsymbol{v_\mu} \times \boldsymbol{b_\nu}$ exceeds $\boldsymbol{E_\phi}$, and for electrons at relativistic energies (>100 keV) does so by more than an order of magnitude. Therefore, because $D_{LL} \propto E^2$, the contribution to D_{LL} from $\boldsymbol{v_\mu} \times \boldsymbol{b_\nu}$ at relativistic energies exceeds that due to $\boldsymbol{E_\phi}$ by a factor $\gtrsim 100$. C2017 estimated peak values of $D_{LL} \lesssim 10^{-4}$ s^{-1} for storm time $\boldsymbol{E_\phi}$ spectra at L=6. The corresponding estimate from the $\boldsymbol{v_\mu} \times \boldsymbol{b_\nu}$ contribution is therefore $\sim 10^{-2}$ s^{-1}. Significantly, the associated diffusive timescale, $\tau_{LL} = 1/D_{LL}$, is less than radiation belt electron drift periods at L=6 for energies up to ~10 MeV and effectively instantaneous relative to the duration of a geomagnetic storm.

To more formally derive D_{LL} we now calculate the displacement of the electron guiding center provided by v_d as defined by Equation 1 in model KFLR wave fields for drift-bounce resonant electrons satisfying Equation 3 at L=6. Further information describing the stochastic approach and its implementation are provided in the supplemental information. The calculation is identical to that performed in C2017, using the same eigenmode solutions of the wave equation for dispersive Alfvén waves [C2017 - Equation 2] to define the wavefields. Except now we consider the $\boldsymbol{v_\mu} \times \boldsymbol{b_\nu}$ contribution to F_ϕ. The wavefields vary as $A(\mu)e^{i(m\phi - \omega t)}$ where $A(\mu)$ describes the amplitude variation with position along geomagnetic field-line. Radial variation could be included however to isolate the physics associated with the local action of $\boldsymbol{v_\mu} \times \boldsymbol{b_\nu}$ we implement here the simplest possible form. The measured fields are modelled as an ensemble of modes with random phases over the broad range of k_ϕ $(or\ m)$ as implied from the dispersion fits in Chaston et al. [2014]. The profile of plasma parameters and b_ν along B_0 corresponding to solutions at a number of $k_\phi \rho_i$ values and harmonics are shown in Figure 2b-f. Here the wavefields are normalized by the amplitude at the equator.

To illustrate how the resonance leads to radial transport Figure 2g presents as an example the azimuthal-latitudinal variation of $\boldsymbol{b_\nu}$ for the 2nd harmonic with $k_\phi \rho_i = 1$ at the equator. We

choose these wave parameters because they allow the clearest demonstration of how the resonance works. The guiding center trajectories shown by the white traces on this panel are provided by the solution of the equation of motion for resonant electrons conserving the 1st adiabatic invariant and having a bounce phase relative to the wave (ψ) of zero with $n = 1$ in Equation 3. Each trace corresponds to a different value of α_{eq}. The resonant energy is ~3 MeV and the azimuthal electron drift and wave phase speed are oppositely directed. The normalized displacement of the guiding center in L (ΔL) experienced by these resonant electrons each bounce is shown in Figure 2h. For a coherent mode the displacement is $N\Delta L$ after N bounces subject to the resonance width in L.

However, because the direction and magnitude of ΔL is dependent on relative bounce and wave phase and the observed wavefields are broadband, net particle transport only occurs on gradients in phase space density and proceeds in a stochastic manner. As an example, Figure 3a shows the phase dependency of ΔL for unperturbed electron orbits at $L = 6$ having α_{eq} =45° and resonant with the 2nd harmonic KFLR. D_{LL} can be estimated numerically from this curve by perturbing a large number of electrons (10000) at this location by ΔL chosen randomly from Figure 3a. This provides a Gaussian distribution of particles in L as shown in Figure 3b after 100 bounces. The diffusion coefficient is then,

$$D_{LL} = \langle(\Delta L)^2\rangle/2\Delta t = \langle(\Delta L_{100})^2\rangle/(2 \times 100\tau_b) \quad (8)$$

where $\langle(\Delta L_{100})^2\rangle$ is provided by the square of the full width at half maximum of the Gaussian distribution. We note that the value for D_{LL} is independent of the number of bounces considered provided this number is sufficiently large. The radial diffusion coefficient derived via this means for $\alpha_{eq} = 45^o$ normalized by the wave magnetic field energy density at the equator is given in Figure 3b. Repeating this process for each pitch angle over a range in equatorial $k_\phi \rho_i$

provides an array of normalized diffusion coefficients $D_{LL}(\alpha_{eq}, k_\phi \rho_i)$ (Figure 3f-h) where each $\alpha_{eq}, k_\phi \rho_i$ pair defines the resonant energy for $n = 1$ in Equation 3 (see Figure 3 c-e).

The morphology of the contour plots shown in Figure 3 f-h for D_{LL} arises from the interplay between the particle trajectory and the profile in $\boldsymbol{b_\nu}$ along B_o. The contours indicate that D_{LL} increases with $k_\phi \rho_i$ and decreases with wave harmonic. The progressive increase with $k_\phi \rho_i$ is a consequence of the corresponding increase in latitudinal extent of the harmonic structure in $\boldsymbol{b_\nu}$ about the equator so that bouncing electrons experience larger wavefields over a greater fraction of a bounce for larger $k_\phi \rho_i$. The decrease of D_{LL} with increasing harmonic number is a consequence of the increasing sign variation of $\boldsymbol{b_\nu}$ along B_o with each larger harmonic. This reduces the net drift across L over a bounce. Finally, the increasing number of peaks in D_{LL} as function of pitch angle with increasing harmonic number arises from the relative location of mirror points along the field and anti-nodes in $\boldsymbol{b_\nu}$**.** With each increase in harmonic number the number of anti-nodes increases so that a proportionate increase in the number of peaks in D_{LL} occurs.

To calculate physical values from the normalized diffusion coefficients presented in Figure 3f-h requires the amplitude at each $k_\phi \rho_i$. This can be evaluated from the observed wave spectrum by associating each spacecraft frame frequency (f_{sc}) with a value for $k_\phi \rho_i$ and deriving the corresponding resonant bandwidth (Δf_{sc}). Figure 4a shows the statistical magnetic field spectrum for the broadband fluctuations reported by Chaston et al., (2015) from the Van Allen Probes while Figure 4b shows the corresponding result for E_{Ysc}/B_{Xsc} in 'sc' coordinates defined in the caption. As indicated above, case studies [Chaston et al., 2014] (including that shown in Figure 1) and statistics [Chaston et al., 2015] show that the superposition of multiple resonances near the equator from the Van Allen Probes provides a trend in E_{Ysc}/B_{Xsc} close to the local dispersion relation for kinetic Alfvén waves. The fit to kinetic Alfvén wave dispersion

here is shown by the red trace. This fit allows each f_{sc} to be identified with a value for $k_\phi \rho_i$ via the dispersion relation. The corresponding amplitude can then be estimated by multiplying the spectral energy density at each $k_\phi \rho_i$ by Δf_{sc} as defined by C2017 for correlation over a bounce as,

$\Delta f_{sc} = f_{sc}/n$ where n=1,2,3… for correlation time, $\tau_c = \tau_b$ (9)

For example, consider the evaluation of D_{LL} for $k_\phi \rho_i = 1$ and $\alpha_{eq} = 45^o$. In Figure 4, $k_\phi \rho_i = 1$ occurs at $f_{sc} = 0.2$ Hz. Using the spectral energy density at this frequency from Figure 4a and multiplying by Δf_{sc}, as given by Equation 9, yields a statistical wave amplitude of ~1 nT. Then taking the normalized value for D_{LL} from the contour plot in Figure 3f for $k_\phi \rho_i = 1$ and $\alpha_{eq} = 45^o$ and multiplying by the amplitude squared provides the physical value, $D_{LL} \approx 10^{-2}$ s^{-1}. The corresponding resonant electron energy for this combination of $k_\phi \rho_i$ and α_{eq} from Figure 3c is ~ 3 MeV. This procedure repeated for all $k_\phi \rho_i$ and α_{eq} provides the arrays of physical values for $D_{LL}(\alpha_{eq}, \mathcal{E})$ at each harmonic shown graphically in Figure 3 i-k.

Figures 3i-k indicate $D_{LL} \gtrsim 10^{-4}$ s^{-1} for energies upward from 100 keV and $D_{LL} \gtrsim 10^{-3}$ s^{-1} above 1 MeV for pitch angles extending from the loss cone to ~80° for the average wave spectra. The increase of D_{LL} with $\mathcal{E}$ evident in Figure 3i-k arises because of the corresponding increase in $\boldsymbol{v_\mu} \times \boldsymbol{b_\nu}$ with energy but also because larger energies resonate at lower $k_\phi \rho_i$ where the wave spectral energy densities are larger. These coefficients correspond to $\tau_{LL} \lesssim 1000$ s for MeV electrons in the average broadband spectrum observed from the Van Allen Probes.

5 Discussion and Conclusions

To quantify the effect of the diffusion coefficients presented in Figures 3h-j on radiation belt populations requires a model for radiation belt phase space density and solution of the radial diffusion equation [Schulz and Lanzerotti, 1974; Eq 3.01]. This goes beyond the scope of this

letter however estimates can be made using Figure 3 where the local profile in phase space density (f) varies as a Gaussian (see Figure 3b). For this case the time rate change of f at location L is given analytically as,

$$f(L,t) \propto \frac{1}{\sqrt{D_{LL}t}} e^{-\frac{(L-L_O)^2}{D_{LL}t}} \quad (10)$$

where L_o is the location of the peak in f. Close to L_o with $t > \tau_{LL}$ we find $f(t) \propto \frac{1}{\sqrt{D_{LL}t}}$. Radiation belt dropouts are characterized by order of magnitude or larger decreases in f [Morley et al., 2010; Turner, 2014]. Such a change in this model therefore requires ~$100\tau_{LL}$. For D_{LL} at $L = 6$ as given in Figure 3h-j, and for energies at and above 1 MeV and $\alpha_{eq} \lesssim 80^o$, we find depletion times of less than a day for the statistical average spectrum of Figure 4a and less than three hours for the storm time spectral energy density shown in Figure 1c. Inclusion of the action of F_μ described earlier through Equations 4-6, but not included in the unperturbed orbit calculations for D_{LL}, indicates that similar time-scales apply even for $\alpha_{eq} > 80^o$. Based on studies by Morley et al., 2010, Turner et al, 2014, Ukhorskiy et al., 2015, Baker et al., 2016, Zhang et al., 2016 and the case study shown in Figure 1 this depletion time is sufficiently short to account for even the most rapid dropouts at this L-shell.

The stochastic interaction is not dependent on the detailed form of the eigenmodes as modelled being replicated in reality. Rather, the key ingredients are the similarity of the range of perpendicular wave scales with the azimuthal electron drift over a bounce period, and the fact that the Alfvénic timescale is much longer than τ_b. This means that the resonance condition (Equation 3) will be satisfied for a broad range of energies and pitch angles to drive bulk radiation belt transport (Figure 3c-e). An individual electron can therefore undergo a continuous series of resonant interactions with different portions of the wave spectrum as it

moves across *L*-shells. Consequently, the broad extent in *L*-shell and longitude of the wave region can be expected to drive bulk transport of radiation belt particles over multiple *L*-shells and local times to account for the broad energy range 'dropout" of the kind shown in Figure 1.

This analysis then indicates that the magnetic fields of broadband low frequency electromagnetic waves during geomagnetic storms will rapidly flatten radial gradients in phase space density. This may lead not only to the depletions/dropouts during main phase, which has motivated this study, but will also drive repopulation during storm recovery as considered by C2017 in the wave electric field. The efficacy of these broadband waves for driving transport and their prevalence during storms suggests they are an important driver of radiation belt dynamics.

Acknowledgments

This research was supported by the NASA Grant numbers NNX15AF57G, NNX16AG69G, NNX17AD36G, NNX17AI55G and Van Allen Probes (RBSP) funding provided under NASA prime contract NAS5-01072; including the EFW and EMFISIS investigations under JHU/APL Contract No.921647 and RBSP-ECT under JHU/APL Contract No. 967399. Data generated from theoretical models is stored on Linux workstations at the Space Sciences Laboratory at UC Berkeley and can be accessed by contacting the first author. Van Allen Probes measurements used in this study can be obtained from the following data repositories: EFW http://www.space.umn.edu/rbspefw-data/; EMFISIS http://emfisis.physics.uiowa.edu/data/index; HOPE/MAGEIS/REPT https://www.rbsp-ect.lanl.gov/science/DataDirectories.php; and/or by directly contacting the first author.

References

Baker, D. N. et al., (2013), The Relativistic Electron-Proton Telescope (REPT) Instrument on Board the Radiation Belt Storm Probes (RBSP) Spacecraft: Characterization of Earth's Radiation Belt High-Energy Particle Populations, Sp. Sci. Rev., DOI 10.1007/s11214-012-9950-9.

Baker, D. N., et al. (2016), Highly relativistic radiation belt electron acceleration, transport, and loss: Large solar storm events of March and June 2015, J. Geophys. Res. Space Physics, 121, 6647–6660, doi:10.1002/2016JA022502.

Balescu, R., Anomalous transport in turbulent plasmas and continuous time random walks, Phys. Rev. E, 51, 4807, 1995.

Born, M. (1949), Natural Philosophy of Cause and Chance, Oxford, Appendix, 20.

Brautigam, D. H., and J. M. Albert (2000), Radial diffusion analysis of outer radiation belt electrons during the October 9, 1990, magnetic storm, J. Geophys. Res., 105, 291–309, doi:10.1029/1999JA900344.

Blake, J. B. et al. (2013), The Magnetic Electron Ion Spectrometer (MagEIS) Instruments Aboard the Radiation Belt Storm Probes (RBSP) Spacecraft, Space Sci Rev, 179:383–421, DOI 10.1007/s11214-013-9991-8.

Chandrasekar, S., (1943) Stochastic Problems in Physics and Astronomy, Rev. Mod. Phys., 15,1.

Chang et al., T., (1986), Transverse acceleration of oxygen ions by electromagnetic ion cyclotron resonance with broad-band left-hand polarized waves, Geophys. Res. Lett., 13, 636.

Chaston, C. C., (2017), Radiation belt dynamics and broadband low frequency electromagnetic waves, 2017 Fall American Geophysical Union Meeting, 11-15 December 2017, New Orleans, Paper Number: 285097.

Chaston, C. C., et al. (2014), Observations of kinetic scale field line resonances, Geophys. Res. Lett. DOI: 10.1002/2013GL058507.

Chaston, C. C., J. W. Bonnell, C. A. Kletzing, G. B. Hospodarsky, J. R. Wygant, and C. W. Smith (2015), Broadband low-frequency electromagnetic waves in the inner magnetosphere, J. Geophys. Res. Space Physics, 120, doi:10.1002/2015JA021690.

Chaston, C. C., J. W. Bonnell, J. R. Wygant, G. D. Reeves, D. N. Baker, D. B. Melrose and Iver. H. Cairns (2017), Radial transport of radiation belt electrons in kinetic field-line resonances, Geophys. Res. Lett., 44, 8140–8148, doi:10.1002/2017GL074587.

Cummings, W. D., R. J. O'Sullivan, and P. J. Coleman Jr. (1969), Standing Alfvén waves in the magnetosphere, J. Geophys. Res., 74(3), 778–793, doi:10.1029/JA074i003p00778.

Dragt, A. J. (1961), Effect of hydromagnetic waves on the lifetime of Van Allen radiation protons, J. Geophys. Res., 66(6), 1641–1649, doi:10.1029/JZ066i006p01641.

Dungey, J., (1964) Effects of electromagnetic perturbations on particles trapped in the radiation belts, Space Sci. Rev., 4, 199-222.

Elkington, S. R., M. K. Hudson, and A. A. Chan (2003), Resonant acceleration and diffusion of outer zone electrons in an asymmetric geomagnetic field, J. Geophys. Res., 108, 1116, doi:10.1029/2001JA009202, A3.

Elkington, S. R. (2006) A Review of ULF Interactions with Radiation Belt Electrons, in Magnetospheric ULF Waves: Synthesis and New Directions (eds K. Takahashi, P. J. Chi, R. E. Denton and R. L. Lysak), American Geophysical Union, Washington, D. C.. doi: 10.1029/169GM12

Fei, Y., A. A. Chan, S. R. Elkington, and M. J. Wiltberger (2006), Radial diffusion and MHD particle simulations of relativistic electron transport by ULF waves in the September 1998 storm, J. Geophys. Res., 111, A12209, doi:10.1029/2005JA011211.

Funsten, H. O. et al., (2013), Helium, Oxygen, Proton, and Electron (HOPE) Mass Spectrometer for the Radiation Belt Storm Probes Mission, Space Sci Rev, DOI 10.1007/s11214-013-9968-7.

Huang, C.-L., H. E. Spence, M. K. Hudson, and S. R. Elkington (2010), Modeling radiation belt radial diffusion in ULF wave fields: 2. Estimating rates of radial diffusion using combined MHD and particle codes, J. Geophys. Res., 115, A06216, doi:10.1029/2009JA014918.

Hudson, M. K., B. T. Kress, H.-R. Mueller, J. A. Zastrow, *and* J. B. Blake *(*2008*),* Relationship of the Van Allen radiation belts to solar wind drivers, J. Atmos. Sol. Terr. Phys., 70*(*5*),* 708–729.

Kletzing, C. A. et al. (2013), The Electric and Magnetic Field Instrument Suite and Integrated Science (EMFISIS) on RBSP, doi: 10.1007/s11214-013-9993-6.

Kulsrud, R.M., and A. Ferrari, (1971) The relativistic quasi-linear theory of particle acceleration by hydromagnetic turbulence, Astrophysics and space science, 12, 302.

Li, X., I. Roth, M. Temerin, J. R. Wygant, M. K. Hudson and J. B. Blake, Simulation of the prompt energization and transport of radiation belt particles during the March 24, 1991 SSC (1993), Geophys. Res. Lett, 22,2423.

Li, Z., M. Hudson, J. Paral, M. Wiltberger, and D. Turner (2016), Global ULF wave analysis of radial diffusion coefficients using a global MHD model for the 17 March 2015 storm, J. Geophys. Res. Space Physics, 121, 6196–6206, doi:10.1002/2016JA022508.

Loto'aniu, T. M., H. J. Singer, C. L. Waters, V. Angelopoulos, I. R. Mann, S. R. Elkington, and J. W. Bonnell (2010), Relativistic electron loss due to ultralow frequency waves and enhanced outward radial diffusion, J. Geophys. Res., 115, A12245, doi:10.1029/2010JA015755.

Mauk, B. H., N.J. Fox, S.G. Kanekal, R.L. Kessel , D.G. Sibeck, A. Ukhorskiy (2012), Science Objectives and Rationale for the Radiation Belt Storm Probes Mission DOI 10.1007/s11214-012-9908-y.

Morley, S. K., R. H. W. Friedel, T. E. Cayton, and E. Noveroske (2010), A rapid, global and prolonged electron radiation belt dropout observed with the Global Positioning System constellation, Geophys. Res. Lett., 37, L06102, doi:10.1029/2010GL042772.

Millan, R. M., and R. M. Thorne (2007), Review of radiation belt relativistic electron losses, JASTP, 69, 362, doi.org/10.1016/j.jastp.2006.06.019

Millan, R. M., K. B. Yando, J. C. Green, and A. Y. Ukhorskiy (2010), Spatial distribution of relativistic electron precipitation during a radiation belt depletion event, Geophys. Res. Lett., 37, L20103, doi:10.1029/2010GL044919.

Millan, R. M., et al. (2012), The Balloon Array for RBSP Relativistic Electron Losses (BARREL), Space Sci. Rev., DOI 10.1007/s11214-013-9971-z.

Nishimura, Y., A. Shinbori, T. Ono, M. Iizima, and A. Kumamoto (2007), Evolution of ring current and radiation belt particles under the influence of storm-time electric fields, J. Geophys. Res., 112, A06241, doi:10.1029/2006JA012177.

Ozeke, L. G., I. R. Mann, K. R. Murphy, I. Jonathan Rae, and D. K. Milling (2014), Analytic expressions for ULF wave radiation belt radial diffusion coefficients, J. Geophys. Res. Space Physics, 119, 1587–1605, doi:10.1002/2013JA019204.

Ozeke, L. G., I. R. Mann, K. R. Murphy, D. G. Sibeck, and D. N. Baker (2017), Ultra-relativistic radiation belt extinction and ULF wave radial diffusion: Modeling the September 2014 extended dropout event, Geophys. Res. Lett., 44, 2624-2633, doi:10.1002/2017GL072811.

Retterer, J. M., Chang, T. and Jasperse, J. R. (1983), Ion acceleration in the supra-auroral region: A Monte Carlo Model. Geophys. Res. Lett., 10: 583–586. doi:10.1029/GL010i007p00583.

Schulz, M., and L.J. Lanzerotti, Particle Diffusion in the Radiation Belts, Springer-Verlag, New York, 1974.

Shprits, Y. Y., R. M. Thorne, R. Friedel, G. D. Reeves, J. Fennell, D. N. Baker, and S. G. Kanekal (2006), Outward radial diffusion driven by losses at magnetopause, J. Geophys. Res., 111, A11214, doi:10.1029/2006JA011657.

Turner, D. L., Y. Shprits, M. Hartinger and V. Angelopoulos (2012), Explaining sudden losses of outer radiation belt electrons during geomagnetic storms electrons during geomagnetic storms, Nature Physics, 8, 208–212, doi:10.1038/nphys2185.

Turner, D. L., et al. (2014), On the cause and extent of outer radiation belt losses during the 30 September 2012 dropout event, J. Geophys. Res. Space Physics, 119, 1530–1540, doi:10.1002/2013JA019446.

Ukhorskiy, A. Y., B. J. Anderson, P. C. Brandt, and N. A. Tsyganenko (2006), Storm time evolution of the outer radiation belt: Transport and losses, J. Geophys. Res., 111, A11S03, doi:10.1029/2006JA011690.

Ukhorskiy, A. Y., M. I. Sitnov, R. M. Millan, B. T. Kress, J. F. Fennell, S. G. Claudepierre, and R. J. Barnes (2015), Global storm time depletion of the outer electron belt. J. Geophys. Res. Space Physics, 120, 2543–2556, doi: 10.1002/2014JA020645.

Wygant, J. R., et al. (2013), The Electric Field and Waves Instruments on the Radiation Belt Storm Probes Mission, Space Sci Rev, DOI 10.1007/s11214-013-0013-7.

Zhang, X.-J., et al. (2016), Physical mechanism causing rapid changes in ultrarelativistic electron pitch angle distributions right after a shock arrival: Evaluation of an electron dropout event, J. Geophys. Res. Space Physics, 121, 8300–8316, doi:10.1002/2016JA022517.

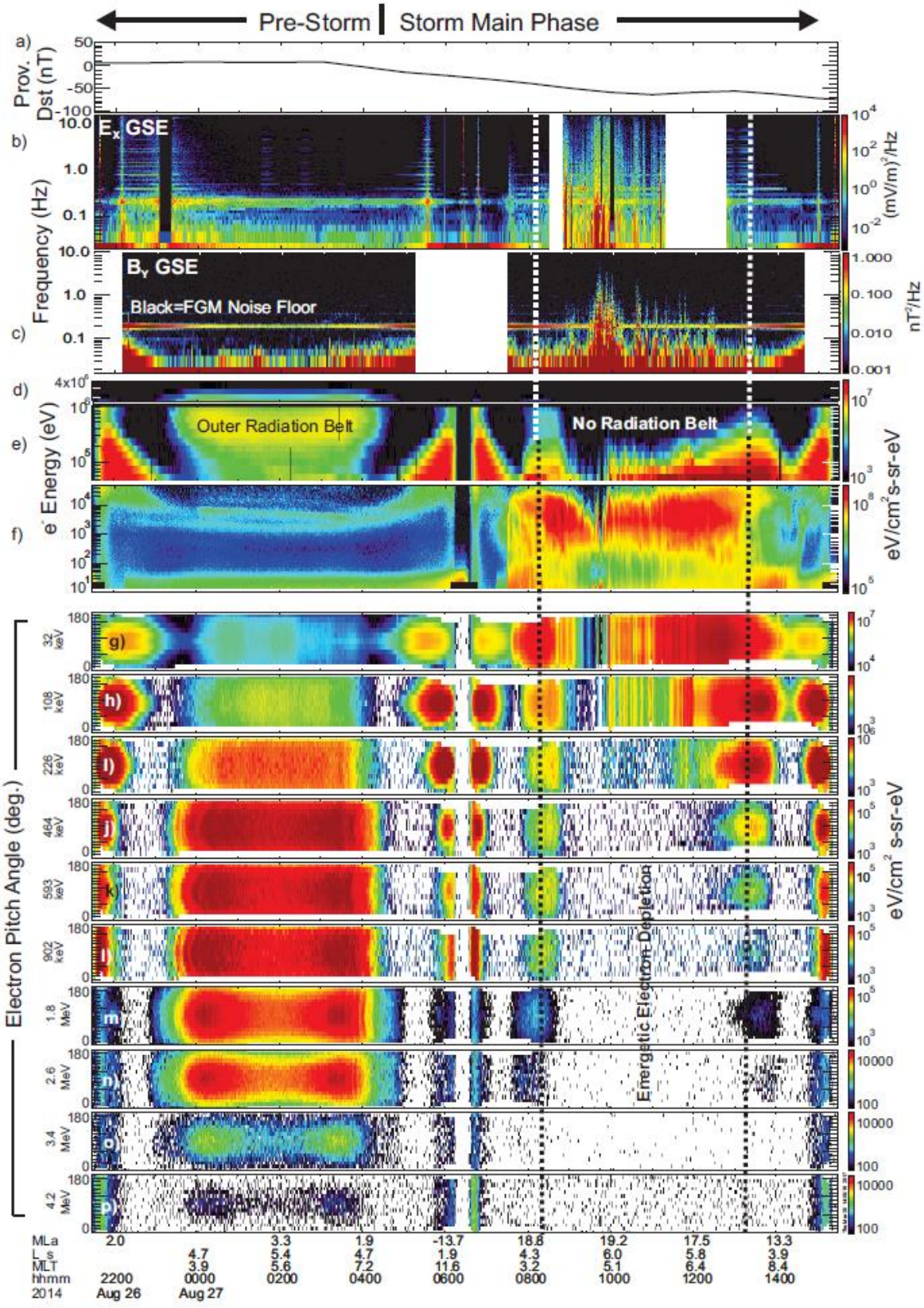

Figure 1. Radiation belt 'dropout' from Van Allen Probe A. a) Dst. b) and c) Azimuthal electric and radial magnetic field spectrograms from EFW (Wygant et al., 2013] and EMFISIS

[Kletzing et al., 2013] respectively. d) Electron differential energy flux spectrogram (1 MeV-4 MeV) from REPT (Baker et al., 2013]. e) Electron differential energy flux spectrogram (50 keV-1 MeV) from MAGEIS [Blake et al., 2013]. f) Electron differential energy flux spectrogram (10 keV-50 keV) from HOPE [Funsten et al., 2013]. g)-p) Electron pitch angle spectrograms from 32 keV to 4.2 MeV.

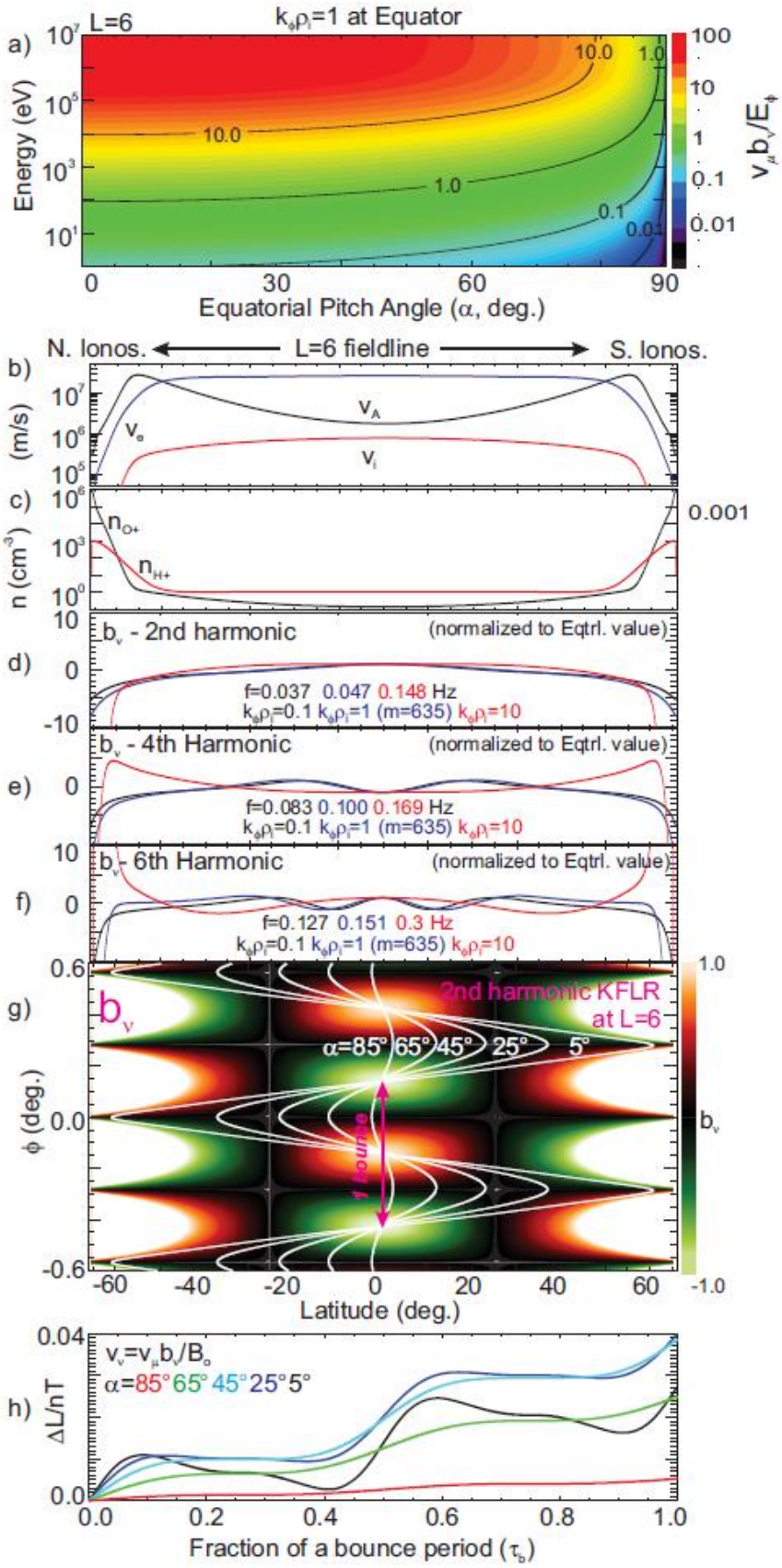

Figure 2. Wavefields and electron orbits at L=6. a) Ratio of Lorentz force due to the wave radial magnetic and azimuthal electric fields ($|v_\mu b_\nu / E_\phi|$) with $k_\phi \rho_i = 1$ at equator. b) Model Alfvén speed, electron and ion thermal speed profiles along the field-line. c) Model H^+ and O^+ densities. d-f) Model radial magnetic field profiles for KFLRs from solution of wave equation (C2017). g) Latitude-Longitude variation of radial magnetic field in 2nd harmonic KFLR with $k_\phi \rho_i = 1$. White traces show trajectory of drift-bounce resonant electrons with n=1 in Equation 3. h) Displacement in L over one bounce normalized by wave amplitude at equator for the resonant electrons shown in panel g.

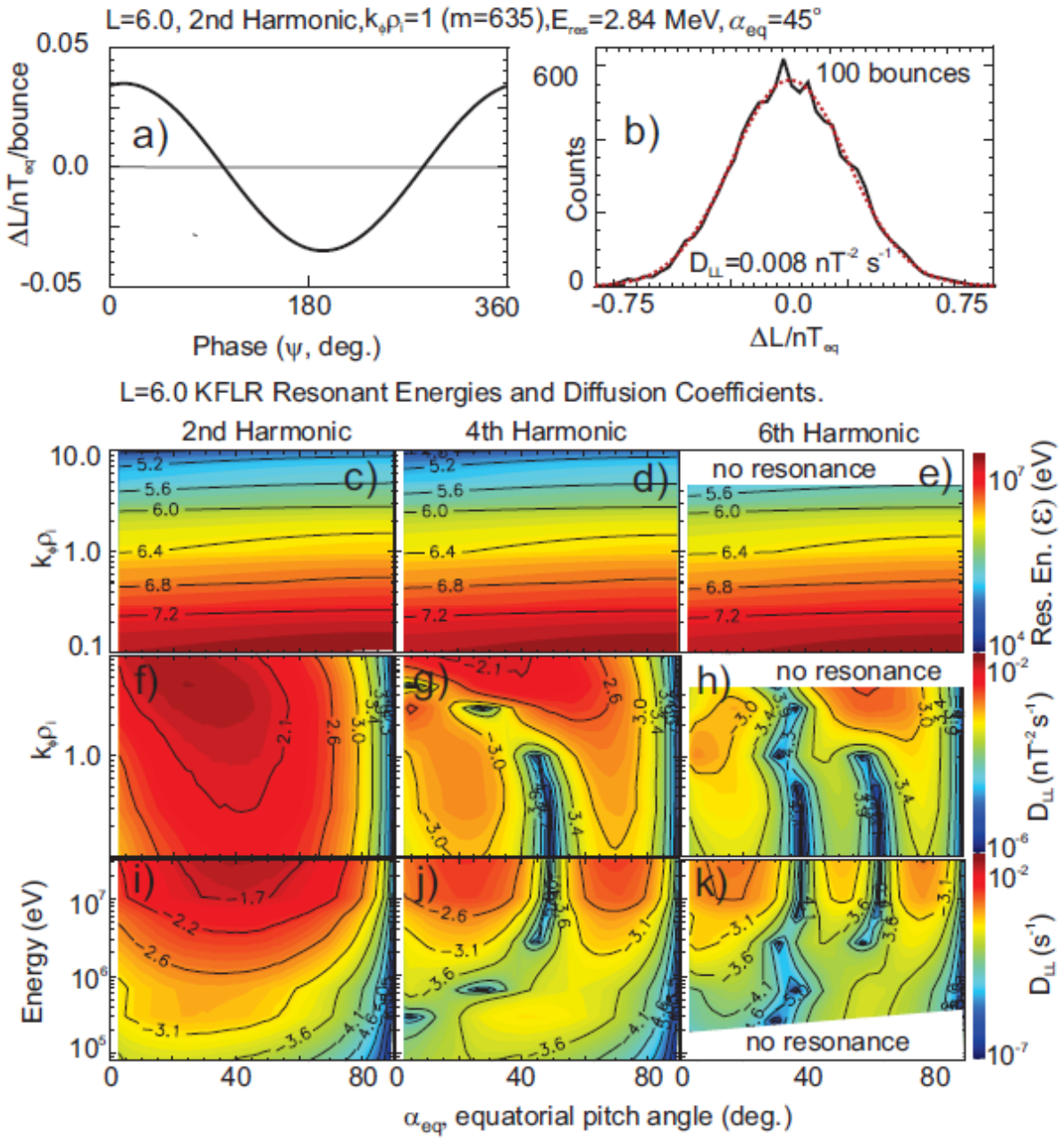

Figure 3. Diffusion at L=6. a) Guiding center displacement as a function of bounce to wave phase. b) Distribution of electron guiding centers in L after 100 bounces from initial population at L=6. c-e) Resonant energies ($\mathcal{E}$) as a function of $k_\phi\rho_i$ and α_{eq} for the 2nd, 4th and 6th harmonics for opposed wave phase velocity and particle drift. f-h). Normalized diffusion coefficients for n=1 in Equation 3. i)-k) Diffusion coefficients for spectral energy densities shown in Figure 4.

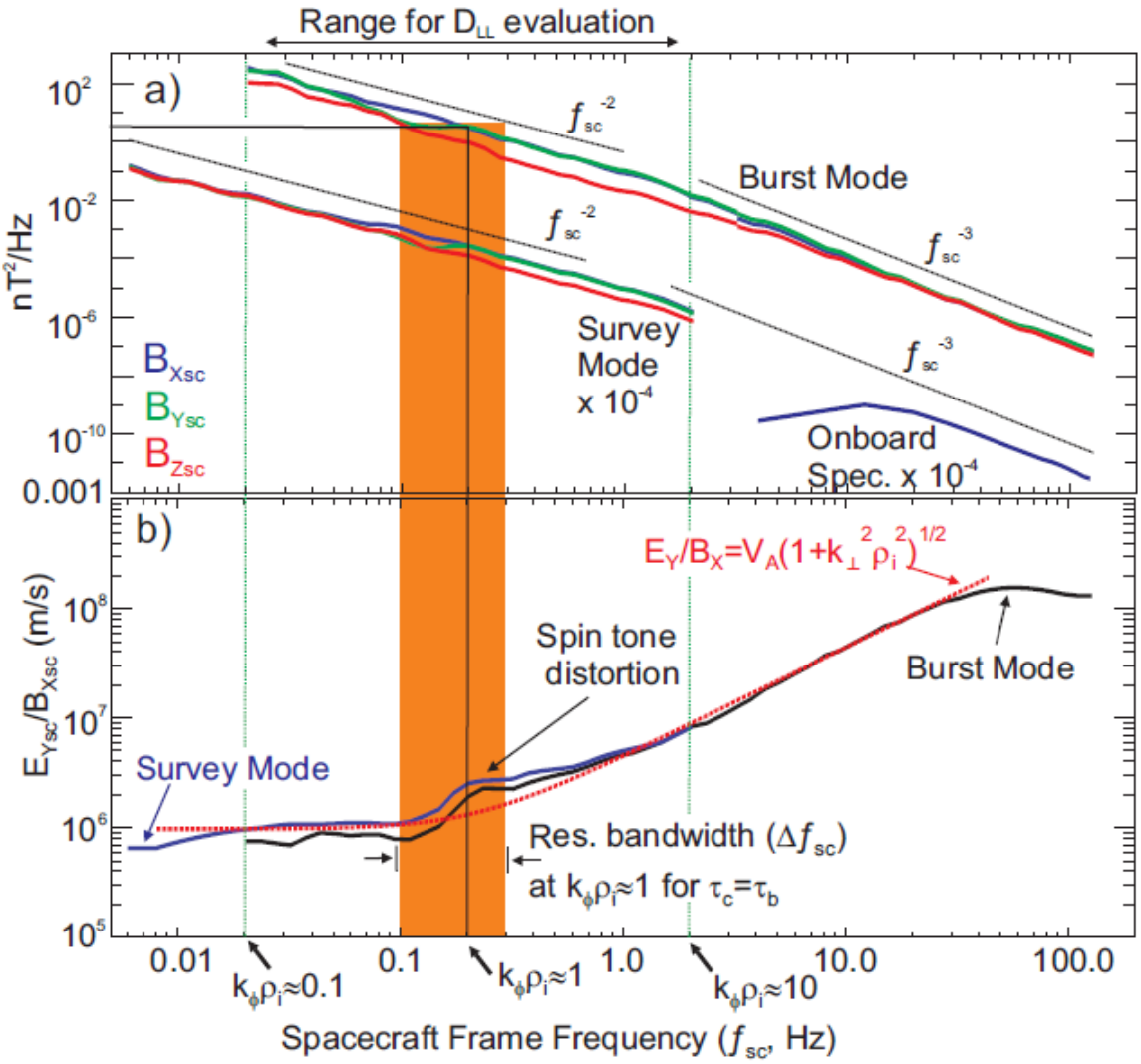

Figure 4. Statistical wave spectra of low frequency broadband electromagnetic waves in field-aligned coordinates from the Van Allen Probes (Chaston et al. [2015]). Z_{sc} is field-aligned while Y_{sc} lies in the spacecraft spin plane. a) and b) spectrum of magnetic field variations and E_{Ysc}/B_{Xsc} respectively. Orange bar shows the resonant bandwidth for a single bounce with $n = 1$ at $k_\phi\rho_i$=1.